Sink of eddy energy by submesoscale sea surface temperature variability in a coupled regional model

Igor Uchoa,[a] Jacob Wenegrat,[a] Lionel Renault,[b]

[a] *Department of Atmospheric and Oceanic Science, University of Maryland - College Park*

[b] *LEGOS, University of Toulouse, IRD, CNRS, CNES, UPS, Toulouse, France*

Corresponding author: Igor Uchoa, iufarias@umd.edu

ABSTRACT: Air-sea interaction impacts ocean energetics via modifications to the exchange of momentum and buoyancy. Prior work at the submesoscale has largely focused on mechanisms related to the eddy kinetic energy (EKE), such as the current feedback on stress, which generates negative wind work, or variations in sea surface temperature (SST) that modify surface winds. However, less is known about the influence of submesoscale SST variability on ocean energetics through its direct effect on the surface flux of eddy potential energy (EPE). Here the role of EPE flux on submesoscale ocean energetics is investigated using a fully-coupled model of the California Current region, including a numerical experiment that suppresses the thermal response in the computation of air-sea fluxes at the submesoscale. Correlations between surface buoyancy anomalies and surface buoyancy fluxes lead to an approximately 10–25% loss of submesoscale EPE, which results in similar magnitude reductions of the vertical buoyancy production, EKE, and eddy wind work. The changes induced by this mechanism in the energy reservoirs and dissipation/conversion pathways are on the same order of magnitude as the negative wind work induced by the current feedback. An approximate form of the EPE flux shows that it is a function of the density ratio and proportional to the surface EPE reservoir of the system. These findings indicate the importance of the submesoscale SST variability, and small-scale variability in surface heat fluxes, in modifying energy reservoirs and conversion pathways of the ocean via the direct flux of EPE at the air-sea interface.

SIGNIFICANCE STATEMENT: This work investigates the impact of small oceanic frontal features in the ocean, classified as submesoscale, in the exchange of energy at the air-sea boundary. Submesoscale fronts and filaments range from approximately 0.1 to 10 km and are characterized by strong horizontal density changes and fast-evolving flow. The associated density anomalies at the surface may be important in the overall energy budget of the surface ocean since they can affect the energy fluxes at the air-sea boundary. Two numerical experiments were set up for a comparative analysis of the energy transfer, conversion, and storage in the upper layer of the California Current region. In one experiment, the role of sea surface temperature anomalies in generating air-sea fluxes is suppressed. A comparison between the two experiments shows a difference of 10-25% in the energy storage and conversion. Sea surface temperature variability may induce a reduction of energy via air-sea fluxes similar to energy dissipation driven by wind-current interactions in the same scale of phenomena.

1. Introduction

The turbulent heat and momentum exchanges across the ocean-atmosphere interface are intrinsically dependent on the scale of the ocean features (Seo et al. 2023). SST variability at the mesoscale plays an essential role in modifying the overlaying atmosphere dynamics which in turn leads to substantial coupled responses of the ocean (Bishop et al. 2017; Chelton and Xie 2010; O'Neill et al. 2012; Small et al. 2008). However, much of our understanding of how ocean variability leads to coupled interactions is constrained to mesoscale resolution (10-100 km). At smaller scales in the ocean, frontal and filamentous features of the order of 0.1-10 km – denoted submesoscale – are characterized by sharper temperature gradients and ageostrophic flows. Submesoscale currents are common oceanic features driven by the downscale eddy cascade of mesoscale flows and are important to global ocean dynamics (McWilliams 2016; Wenegrat et al. 2018). As the dynamics of submesoscale currents are strongly ageostrophic, strong vertical velocities are characteristic in the flow which allow for strong transport of properties such as dissolved gases, nutrients, and heat (Mahadevan et al. 2012; Renault et al. 2016; Balwada et al. 2021). The vertical flux of heat (buoyancy) affects both the timing and strength of ocean stratification (Mahadevan et al. 2012; Johnson et al. 2016) and the surface flux of heat between the ocean and atmosphere (Su et al. 2018, 2020; Iyer et al. 2022).

Air-sea interaction at the submesoscale is somewhat less well understood since numerical simulations are computationally costly and observations are challenging. Observation works that have investigated the air-sea fluxes at the submesoscale, although scarce, have shown larger fluxes of heat, moisture, and momentum at fronts (Shao et al. 2019; Iyer et al. 2022), also consistent with submesoscale-permitting global ocean models analysis that used uncoupled air-sea bulk formulae (e.g., Su et al. 2018, 2020). Coupled numerical simulations have shown an active EKE transfer at the air-sea interface by submesoscale variations in surface wind stress (e.g., Renault et al. 2018; Bai et al. 2023; Conejero et al. 2024). For example, coupled modeling experiments of the California Current System indicate that modifications to the wind stress by small-scale currents (the current feedback on stress, CFB) lead to a 17% reduction in submesoscale EKE (Renault et al. 2018). These changes to the surface stress also modify the Ekman transport of buoyancy at fronts, and consequently the PV budget of the surface mixed-layer (Wenegrat 2023). In addition, modulations of the marine atmospheric boundary layer and changes in atmospheric kinetic energy by SST variability, namely, the thermal feedback mechanism (TFB), were also explored in idealized models (Wenegrat and Arthur 2018; Sullivan et al. 2020, 2021). These results indicate that sharp fronts at the submesoscale impact the response of the marine atmospheric boundary layer by driving secondary circulations in the atmosphere which in turn modify the surface wind stress and wind work (Skyllingstad et al. 2007; Wenegrat and Arthur 2018; Sullivan et al. 2021). Recent studies also show the combined effect of CFB and TFB in the wind stress (Bai et al. 2023; Conejero et al. 2024), which indicates that submesoscale SST variability shows a direct influence on the transfer of momentum between the atmosphere and ocean, modifying the surface flux of EKE.

The influence of submesoscale SST variability on ocean energetics through its direct effect on the surface flux of EPE, however, is less explored. Observations show strong covariability between surface heat fluxes and surface buoyancy anomalies at the submesoscale (Shao et al. 2019; Iyer et al. 2022; Yang et al. 2024), suggesting there will also be a direct surface flux of EPE. This has been shown to be an important sink of mesoscale EPE (Bishop et al. 2020; Guo et al. 2022), which can impact the baroclinic conversion rate in boundary currents in the first 100 m of the upper ocean (Ma et al. 2016; Renault et al. 2023), but has not yet been explored at the submesoscale. Here we investigate the impact of SST anomalies on submesoscale EPE flux using a fully-coupled regional model of a portion of the California Current system, a region where submesoscale features have been indicated as important drivers of air-sea fluxes as momentum and heat (Capet et al. 2008b; Renault et al. 2018).

Two coupled ocean-atmosphere simulation setups are used to assess the effect of submesoscale SST variability on the EPE flux, including both a fully coupled simulation and one where submesoscale SST anomalies are not included for air-sea flux calculations. The flux, conversion, and storage components of eddy energy in the mixed layer for both simulations are compared, highlighting an increase of eddy energy when SST anomalies do not affect surface fluxes. The impact of the EPE flux is not limited to the EPE but also propagates to changes in EKE through modification of the vertical buoyancy production and changes to the surface wind work. This analysis shows that the flux of EPE driven by SST at the submesoscale is comparable to analogous transfers of EKE by surface momentum transfer (wind work) at the submesoscale.

The work is organized as follows. Section 2 introduces the theoretical background for the eddy energy equations in spectral space. The numerical experiments are described in section 3. In section 4, the submesoscale dynamics of the numerical simulations are described, and the impact of the surface EPE flux is estimated. An approximated form of the EPE flux is obtained and compared with the flux of EKE by the surface wind work in section 5. Finally, the results are summarized in section 6.

2. Energy equations and spectral analysis

a. Eddy potential energy and eddy kinetic energy equations

This work compares the eddy energy pathways and reservoirs of the upper ocean, assessing the influence of submesoscale SST anomalies in the air-sea fluxes variability. We consider the reservoirs, conversion rates, and flux terms of eddy energy in horizontal wavenumber space. The mixed-layer integrated EPE and EKE equations for a Boussinesq fluid in spectral space are written as

$$\int_{z_m}^{0} \frac{\partial}{\partial t} EPE\, dz = \int_{z_m}^{0} \Big(- A_b - C_{(EKE,EPE)} + V_b \Big)\, dz, \tag{1}$$

$$\int_{z_m}^{0} \frac{\partial}{\partial t} EKE\, dz = \int_{z_m}^{0} \Big(- A_m - PH + C_{(EKE,EPE)} + V_m \Big)\, dz, \tag{2}$$

where the left-hand side terms represent the rate of change of EPE and EKE integrated from the surface to the mixed layer depth (z_m). The eddy terms analyzed in this work refer to the variability encompassed at the small mesoscale and submesoscale horizontal wavenumbers (see section 3c). The reservoirs are described as follows

$$EPE = \mathbb{R}\left[\frac{\widehat{b}\,\widehat{b^*}}{2N_r^2}\right], \tag{3}$$

$$EKE = \mathbb{R}\left[\frac{\widehat{u}\,\widehat{u}^* + \widehat{v}\,\widehat{v}^*}{2}\right], \tag{4}$$

where b is buoyancy, $N_r^2 = \frac{\partial <b>}{\partial z}$ is the reference squared Brunt Vaissala frequency (i.e., $< b >$ is the horizontally and temporally averaged buoyancy), and u and v are the zonal and meridional velocity components. The caret $\widehat{(.)}$ denotes the two-dimensional Fourier transform. The symbol $\mathbb{R}$ represents the real component of the spectra and the asterisk (*) indicates the complex conjugate operator.

The A_b term in (1) and the A_m term in (2) include the horizontal advection of EPE and the 3D advection of EKE, respectively. Those terms also include the cross-scale fluxes of energy which are not analyzed here due to domain size constraints (briefly discussed in section 6). The PH term in (2) represents the pressure work, also not described in this work.

The rate of conversion between EPE and EKE, $C_{(EKE,EPE)}$, is

$$C_{(EKE,EPE)} = \mathbb{R}\{\widehat{w}\widehat{b^*}\} \tag{5}$$

where w represents the vertical velocity component. Conversion of EPE at the submesoscale is generated by baroclinic mixed-layer instabilities and other ageostrophic secondary circulations that extract available potential energy from fronts (Fox-Kemper et al. 2008).

The V_b term in (1) arises from the diffusive term in the buoyancy budget, and hence once integrated over the mixed-layer contains contributions from both the dissipation of EPE and the diffusive fluxes of EPE at the surface and mixed-layer base (detailed derivation in Appendix A). The surface EPE flux is the focus of this work, which can be determined using the surface boundary condition (Cronin and Sprintall 2001; Storch et al. 2012)

$$\kappa \frac{\partial}{\partial z} b \bigg|_{z=0} = B_o, \tag{6}$$

where κ is the vertical diffusivity and B_o is the surface buoyancy flux. The EPE flux, hereafter referred to as G_{EPE}, is then

$$G_{EPE} = \mathbb{R}\left[\frac{\widehat{b_o^*}\widehat{B_o}}{N_r^2}\right] \tag{7}$$

where b_o is the surface buoyancy. Negative G_{EPE} values indicate EPE loss from the ocean, whereas positive G_{EPE} indicates a gain of EPE.

Analogously, the diffusive flux of EKE at the surface (or wind work) may be calculated by vertically integrating V_m and using the surface boundary conditions for momentum (more details of the derivation in Capet et al. 2008b; Storch et al. 2012). The wind work, G_{EKE}, is thus defined as

$$G_{EKE} = \frac{1}{\rho_o}\Big(\mathbb{R}\big[\,\widehat{\tau_x}\,\widehat{u_o^*} + \widehat{\tau_y}\,\widehat{v_o^*}\big]\Big), \tag{8}$$

where ρ_o is the background surface density, $\boldsymbol{\tau} = (\tau_x, \tau_y)$ is the surface momentum flux, and $\boldsymbol{u}_o = (u_o, v_o)$ is the surface velocity, with the zonal and meridional velocity components, respectively.

3. Numerical simulation

a. Model description

The ocean components of the coupled model in the California Current System region use the Regional Oceanic Modeling System (ROMS) in its CROCO version (Coastal and Regional Oceanic COmmunity) (Shchepetkin and McWilliams 2005; Debreu et al. 2012; Shchepetkin 2015). CROCO is a free-surface, terrain-following coordinate model with split-explicit time stepping. The equations solved in this model's configurations were set for Boussinesq and hydrostatic approximations. The numerical experiments used in this work are the highest resolution products from a four nest configuration described in Renault et al. (2018). The domain for the simulations covers 119.9° W to 128.98° W and from 32.54° N to 40.73° N (Fig. 1). The simulations were spun up from the same initial state from June to November 2011, after which they were run separately

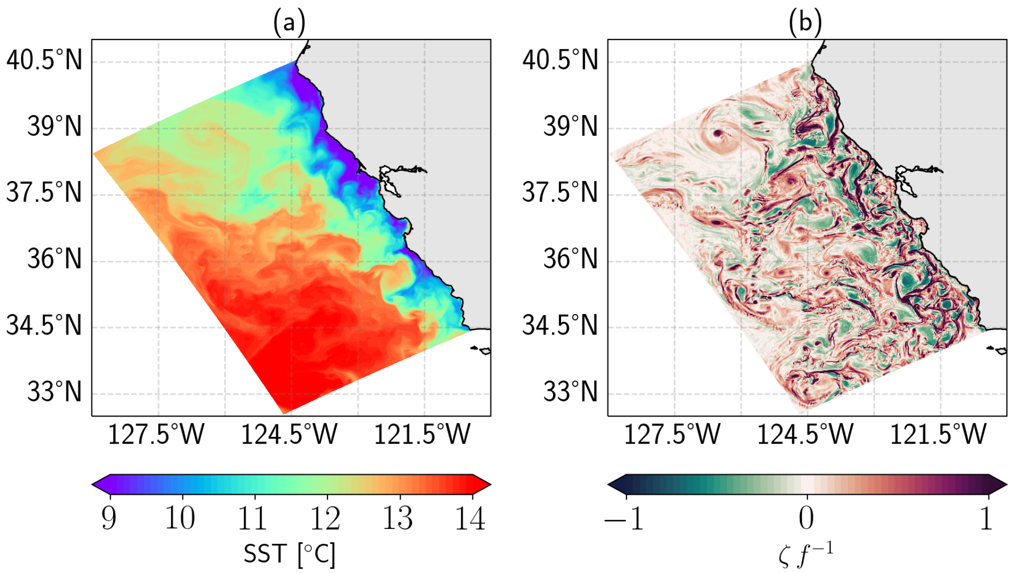

Fig. 1. Snapshots of (a) sea surface temperature and (b) surface vorticity normalized by the Coriolis frequency (f) from the fully coupled simulation illustrating the model domain.

from November 2011 to June 2012 (more detailed description in section 3b). The boundary and initial conditions are taken from a coarser 4-km nested grid. For the horizontal grid, 1000 × 1520 points with a grid spacing of (Δx, Δy) = 0.5 km were set with 80 terrain-and-surface-following sigma levels in the vertical with stretching parameters hcline = 200 m, $\theta_b = 3.0$, and $\theta_s = 6$. The turbulence closure used is the K-Profile Parameterization (KPP, Large et al. 1994). The outputs analyzed in this work have a 6-month time span (January to June 2012) with a 6-hour temporal resolution. More information about the settings and spin-up of the model can be found in Renault et al. (2018).

For the atmospheric component of the fully-coupled system, the Weather Research and Forecast Model (WRF, version 4.1) was used (Skamarock et al. 2019). An implementation of a nesting grid is also used in this model as in Renault et al. (2018). The atmospheric component used in this work has a spatial resolution of 2 km with initial and boundary conditions provided by the simulation from the previous nesting with a 6 km horizontal resolution. The domain for the simulations covers 118.98° W to 129.14° W and from 32.44° N to 41.20° N, which is slightly larger than the ocean domain to avoid the WRF sponge boundaries. For the horizontal grid, 300 × 390 points with a grid spacing of (Δx, Δy) = 2 km were set with 50 vertical levels. In the boundary layer model, bulk formulae (COARE formulation, Edson et al. 2013) are used to compute the surface turbulent heat, freshwater, and momentum fluxes, which are subsequently provided to CROCO. Note that, in this work, the implementation used of a surface-layer vertical mixing parameterization for the planetary boundary layer (MYNN, Nakanishi and Niino 2006) and a tri-diagonal matrix for vertical turbulent diffusion is necessary for the implementation of relative winds in the atmospheric model and to reproduce the CFB mechanism appropriately (Renault et al. 2019).

The OASIS3 software was used for the surface data exchange between the two models (Valcke 2013) to couple CROCO and WRF. This procedure supports the communication of two-dimensional fields between the two numerical codes for the integration of the coupled system. The diagram in Fig. 2 illustrates the surface fluxes computation using this software. In these experiments, WRF provides the hourly averages of freshwater, heat, and momentum fluxes to CROCO whereas CROCO feeds the hourly SST and surface currents to WRF for the calculation of fluxes. OASIS3 is implemented in the 4 km and 6 km grids for CROCO and WRF, respectively, and nested into the higher resolution grids.

b. Experiment setup

To observe the impacts of SST variability at the submesoscale on the upper ocean dynamics, two fully-coupled numerical simulations were implemented using two different air-sea coupling configurations. A schematic of the two experimental setups is illustrated in Fig. 2. The first experiment consists of a fully-coupled model system, hereafter referred to as the FULL experiment. In the second experiment, SST anomalies are low-pass filtered before being passed to WRF for the calculation of surface fluxes, suppressing the role of submesoscale SST variability in air-sea interaction as illustrated in Fig. 2. The latter experiment will be referred to as the SMTH experiment. This comparison between experiments assesses the impact of the ocean submesoscale SST variability on the exchange of heat and momentum at the air-sea interface. This analysis is similar to previous studies performed in mesoscale-resolving simulations (Zhai and Greatbatch 2006; Seo et al. 2016; Renault et al. 2023).

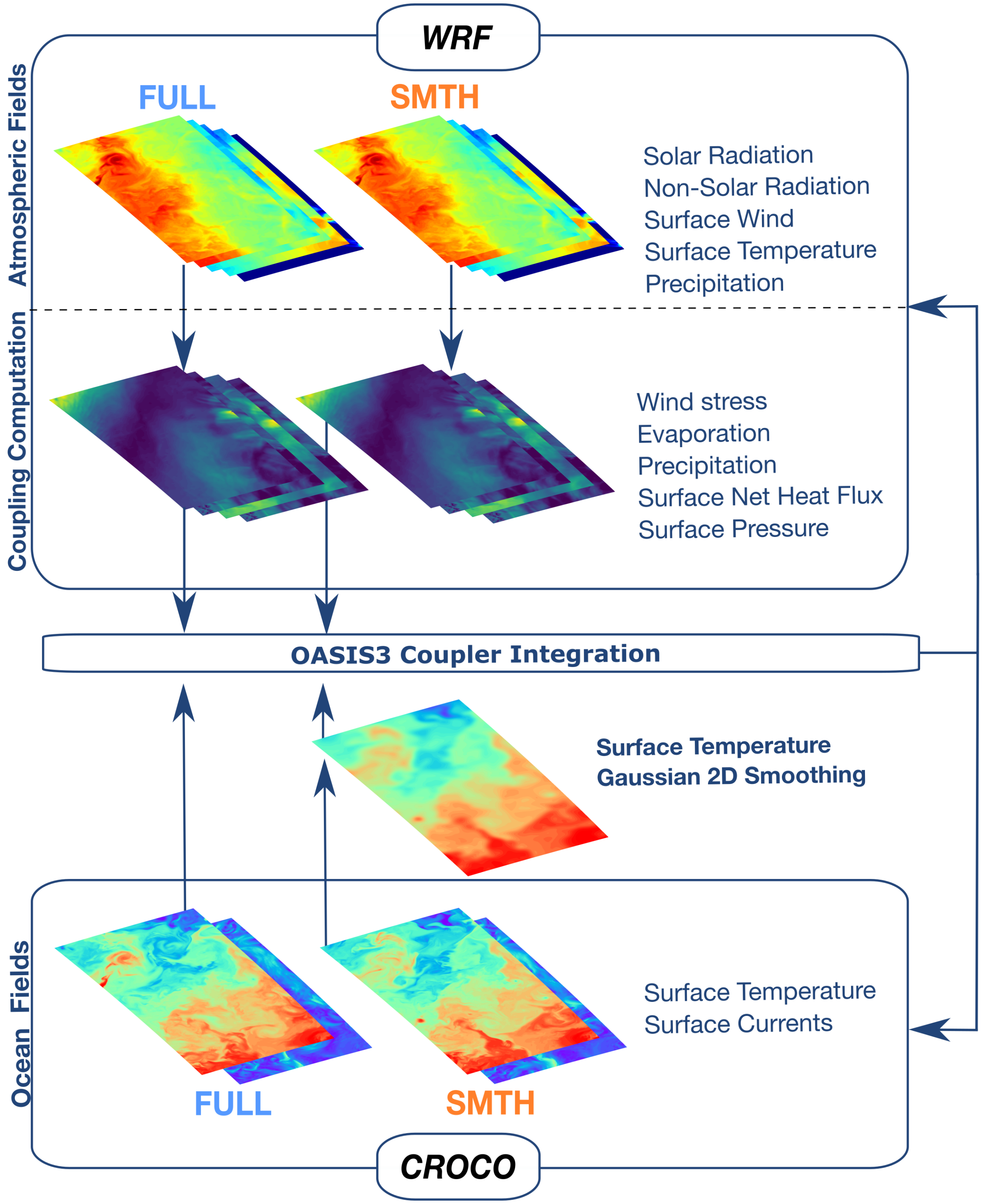

FIG. 2. Schematics of the different coupling computations for the FULL and SMTH experiments using WRF (The Weather Research and Forecast Model) and CROCO (Coastal and Regional Ocean COmmunity Model). The examples illustrate the computation of sensible heat flux. The filtering of submesoscale sea surface temperature variability for the coupling computation is illustrated for the SMTH experiment.

c. Spatial filtering and spectral analysis

A two-dimensional spatial Gaussian filter is used to isolate submesoscale anomalies from the mesoscale and large-scale signals. The filter applies a $(6\sigma + 1)$ window in both horizontal dimensions and has a σ=3 and a cutoff value of 0.5 as performed in Renault et al. (2023). This configuration allows for an assessment of the impact of SST submesoscale anomalies in the energy fluxes, reservoirs, and conversion rates. In Fig. 3 an example of the differences in the SST field used in the air-sea coupling between simulations is shown. The filter reduces variability from approximately 50 km wavelength (0.02 km^{-1} wavenumber) to smaller scales, such that at 20 km wavelength (0.05 km^{-1} wavenumber) SST variability is reduced by an order of magnitude. Here we refer to the range of scales smaller than this filter scale as 'submesoscale' however we note that the submesoscale is more accurately defined as a dynamical regime, and hence the definition employed here is only approximate. The Fourier transform calculation in this work includes subtraction of the spatial mean and tapering using a Hanning window. A temporal average of the period of the simulations (i.e., 6 months) is also applied in all spectra.

4. Results

a. Model characterization

The submesoscale dynamics of the California Current are depicted in Fig. 1 where SST and normalized relative vorticity fields (i.e., Rossby number) show strong variability in the region. Smaller-scale vortices and their associated high normalized relative vorticity, $Ro \sim O(1)$, indicate the presence of flows that are dynamically submesoscale, a consequence of mesoscale strain and frontal instabilities of the California Current (Capet et al. 2008a).

The surface eddy energy reservoirs, vorticity, and divergence are impacted by air-sea fluxes driven by SST anomalies at the submesoscale as shown in Fig. 4. The SMTH experiment has more eddy energy (in both EPE and EKE) than the FULL simulation that accounts for submesoscale SST variability in air-sea fluxes (Fig. 4a). This surplus of energy indicates more variability in velocity and buoyancy at the submesoscale when air-sea fluxes driven by SST anomalies are suppressed. Both EPE and EKE surface spectra present a slope of $\sim k_h^{-2}$ which is associated with flows with energetic submesoscale currents (Capet et al. 2008a) and a white horizontal gradient spectra. The EKE spectral slope found is similar to observations in adjacent regions such as the

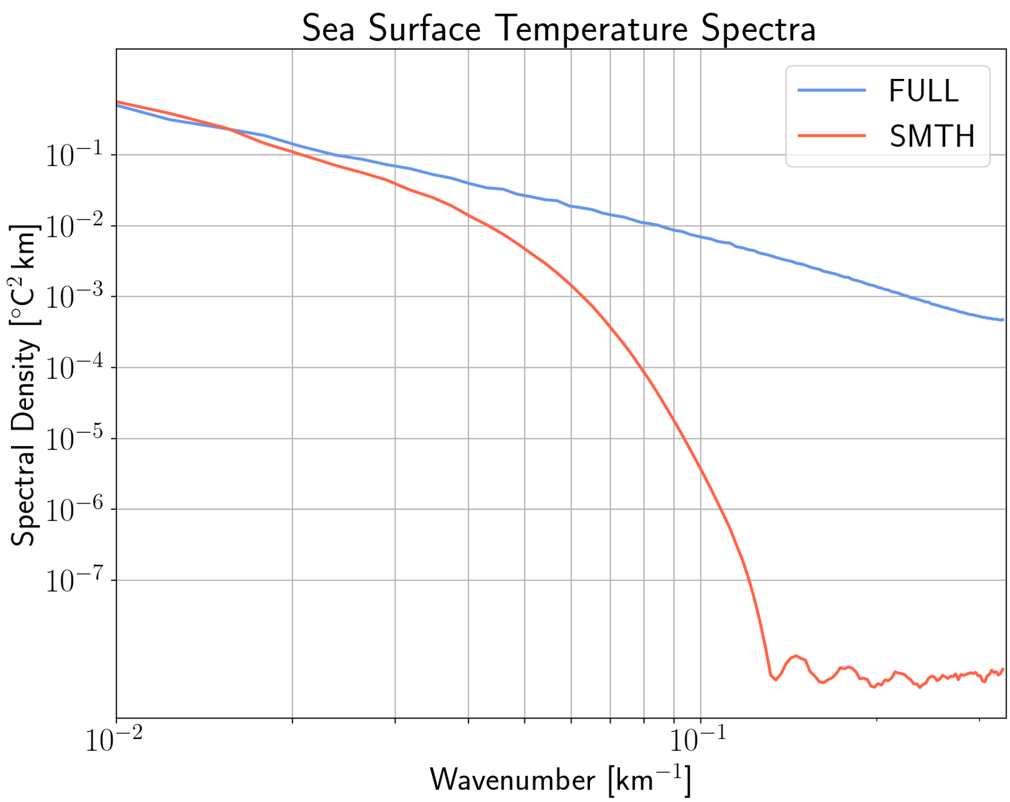

FIG. 3. Isotropic wavenumber spectra comparing the sea surface temperature fields in the coupling computation for the model simulation setups FULL and SMTH.

Southern California Current (Chereskin et al. 2019), which attributes the behavior to an energetic submesoscale and relatively weaker mesoscale than in Western Boundary Currents. Vorticity (ζ) and divergence (δ) spectra are proportional to the horizontal velocity gradient, which indicate sharp velocity gradients commonly observed in submesoscale fronts and filaments (Barkan et al. 2019). Fig. 4b indicates weaker velocity gradients in the FULL experiment compared to the SMTH case.

b. Eddy potential energy flux at the submesoscale

SST anomalies at the submesoscale enhance the loss of EPE via correlations between the thermal components of buoyancy and buoyancy flux. A schematic representation of the mechanism above is shown in Fig. 5 where spatial anomalies of buoyancy (b') and buoyancy flux (B'_o) are correlated. The heat flux anomalies respond to SST anomalies at the front to diminish the differences in temperature between the surface ocean and the atmosphere. This mechanism decreases the absolute

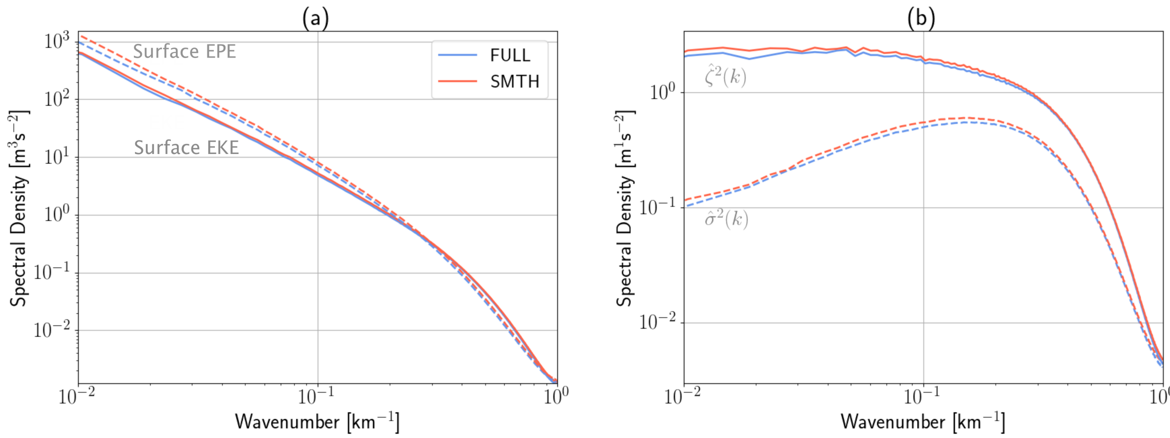

FIG. 4. Surface dynamics and energetics are influenced by air-sea fluxes at the submesoscale. Two-dimensional spectra of surface (a) eddy kinetic energy (EKE) and eddy potential energy (EPE), and (b) vorticity (ζ) and divergence (σ) for the FULL (blue line) and SMTH (orange line) simulation outputs.

values of b' and hence the mixed-layer EPE (assuming temperature anomalies and buoyancy anomalies are of the same sign, discussed further in section 5).

The air-sea buoyancy flux, B_o, may be parameterized as proportional to heat and freshwater fluxes (Cronin and Sprintall 2001):

$$B_o = \frac{\alpha_\theta g}{\rho_o C_p} Q_{net} - \beta_S g S_o (E - P), \tag{9}$$

where g is gravity, S_o is the surface salinity, C_p is the specific heat of water, Q_{net} is the net surface heat flux, E is evaporation and P is precipitation. α_θ and β_s represent the thermal expansion and salinity contraction coefficients calculated at each point. This parameterization allows for the computation of G_{EPE}.

The spectra of G_{EPE} are shown in Fig. 6. The loss or gain of EPE in the ocean is represented as negative and positive spectral density values, respectively. The co-spectra of the surface buoyancy and buoyancy flux (G_{EPE}) show a difference in EPE flux exceeding an order of magnitude between the SMTH and FULL experiments. The FULL experiment spectrum shows loss of EPE in the submesoscale and lower mesoscale spatial range, which indicates that submesoscale EPE flux is working as a sink of energy to the atmosphere, similar to mesoscale SST anomalies (Storch et al. 2012; Bishop et al. 2020; Guo et al. 2022; Renault et al. 2023). Conversely, the SMTH experiment

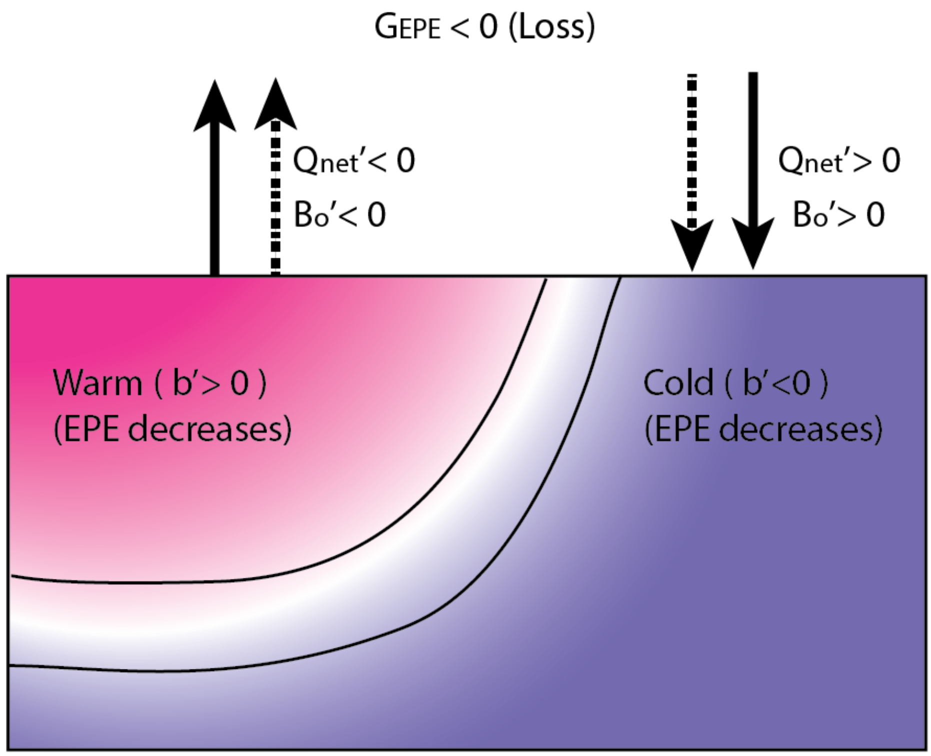

FIG. 5. Schematic representation of the surface flux of EPE driven by SST anomalies and heat flux in a submesoscale front. Heat flux counteracts the SST anomalies, resulting in a decrease in buoyancy anomaly on both sides of the front and an overall loss of EPE. The prime symbol represents the spatial anomalies due to the front.

spectrum indicates a gain of EPE flux at the submesoscale and a smaller loss at the small mesoscale range compared to the FULL experiment. The gain of EPE, G_{EPE} >0, likely occurs in the SMTH simulation because the heat flux is not necessarily driven by SST anomalies and thus may act to enhance the buoyancy anomalies' magnitude, increasing the EPE. These differences in EPE flux between the numerical experiments indicate that submesoscale air-sea fluxes are acting as a sink of submesoscale EPE.

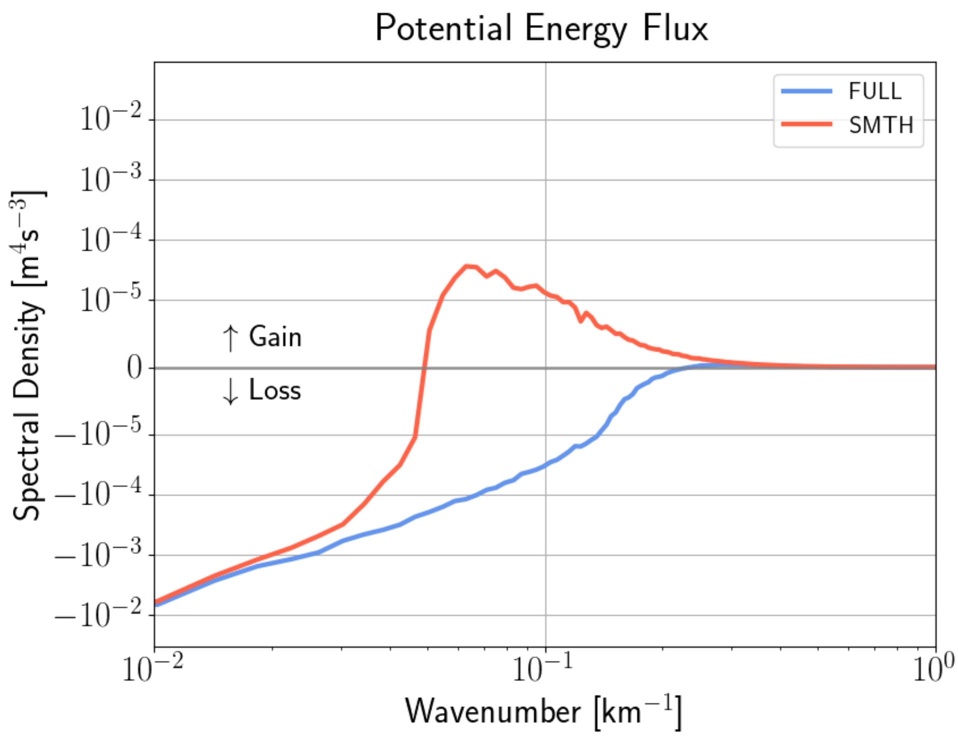

FIG. 6. Submesoscale buoyancy anomalies are correlated with buoyancy flux anomalies, driving a loss of EPE to the atmosphere. Two-dimensional spectra of available potential energy flux for the FULL (blue line) and SMTH (orange line) experiments. The spectra are averaged over time period of the simulations. Positive (negative) values represent the gain (loss) of EPE to the atmosphere.

c. Decomposition of eddy potential energy flux and approximations

The G_{EPE} term is further expanded to assess the importance of each component contributing to b and B_o anomalies. It is possible to approximate surface buoyancy into a linear equation that takes into account SST and salinity anomalies and surface values of α_θ and β_S. The linearized surface buoyancy in spectral space is:

$$\widehat{b_o} \approx g\left[\,\widehat{\alpha_\theta T_o} - \widehat{\beta_S S_o}\,\right]. \tag{10}$$

where T_o is the surface temperature.

Using (10) and (9), the EPE flux can be divided into components driven by thermal and salinity anomalies and fluxes. This decomposition allows for the assessment of the relative contributions of surface temperature and salinity anomalies and fluxes of heat and freshwater in G_{EPE}. The expansion can be written as

$$G_{EPE} \approx \frac{1}{N_r^2}\mathbb{R}\left[\widehat{b_T}^*\widehat{B_{oT}} + \widehat{b_T}^*\widehat{B_{oS}} + \widehat{b_S}^*\widehat{B_{oS}} + \widehat{b_S}^*\widehat{B_{oT}}\right], \tag{11}$$

where the components of buoyancy and buoyancy flux are defined as follows:

$$\widehat{b_T} = g\,\widehat{\alpha_\theta T_o}, \tag{12}$$

$$\widehat{b_S} = -g\,\widehat{\beta_S S_o}, \tag{13}$$

$$\widehat{B_{oT}} = \frac{g}{\rho_o C_p}\,\widehat{\alpha_\theta Q_{net}}, \tag{14}$$

$$\widehat{B_{oS}} = -g\widehat{\beta_S (E-P) S_o}, \tag{15}$$

The total EPE flux thus consists of components from correlations between surface temperature anomalies and heat fluxes, surface salinity anomalies and freshwater fluxes, and cross-terms (eg. correlations between surface heat fluxes and salinity anomalies). The spectra for the four components for the FULL experiments are shown in Fig. 7. G_{EPE} components correlated with temperature anomalies (i.e., b_T, Fig. 7 - red lines) indicate a net loss of EPE to the atmosphere, whereas the components generated by salinity anomalies (i.e., b_S, Fig. 7 - blue lines) show a net gain of EPE. The product of the thermal components of buoyancy and buoyancy flux (i.e., $b_T B_{oT}$, Fig. 7 - red solid line) is the dominant component of EPE flux to the atmosphere at the submesoscale and is responsible for the net loss of EPE shown in Fig. 6. The term that correlates the salinity component of buoyancy and buoyancy fluxes (i.e., $b_S B_{oS}$, Fig. 7 - blue solid line) has the smallest magnitude at the submesoscale, indicating that B_{oS} (proportional to freshwater fluxes) is not as efficient as B_{oT} (proportional to heat fluxes) in fluxing EPE in this region. Instead, the component that contributes to the largest gain of EPE in the analysis is the cross-term $b_s B_{oT}$ (Fig. 7 - dashed blue line). Temperature and salinity anomalies drive inverse changes in the EPE of the upper ocean, which as shown below results from the partial density compensation of fronts in the California Current Region (Rudnick and Ferrari 1999; Mauzole et al. 2020). B_{oT} may also be further approximated to the latent and sensible components of heat flux anomalies since those

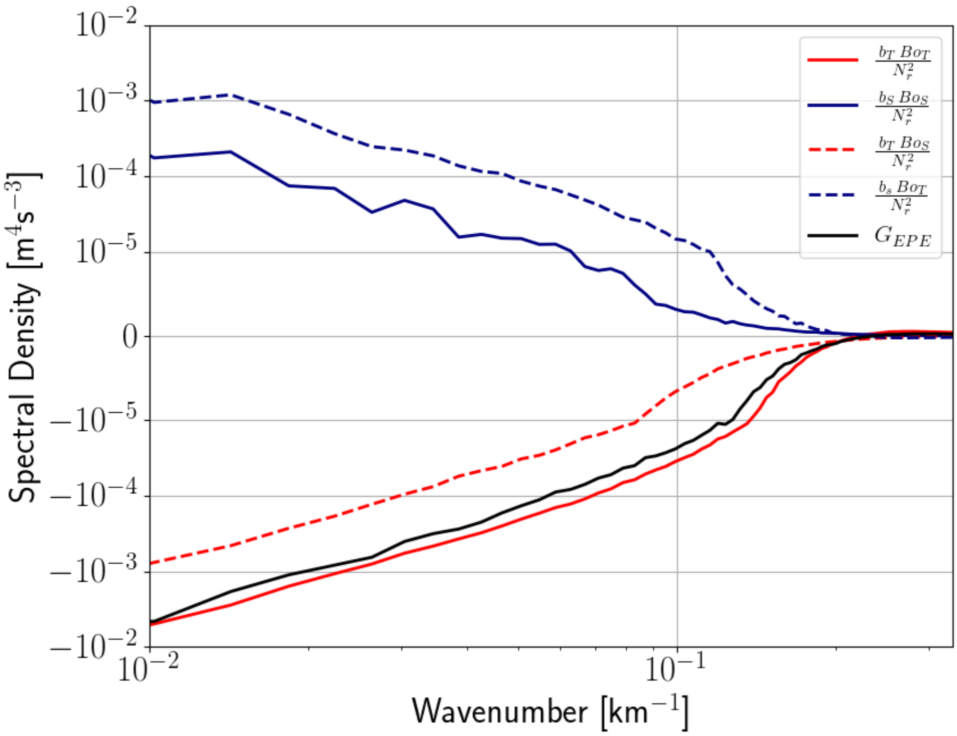

FIG. 7. Correlation between heat flux and surface buoyancy anomalies has the greatest contribution to the EPE flux. Decomposition of the total EPE flux (FULL) in terms of the contributions of temperature and salinity components (see section 4c). Blue lines represent the components of G_{EPE} proportional to salinity anomalies (b_S). Red lines represent the components proportional to temperature anomalies (b_T). The solid blue and red lines represent the component proportional to temperature and heat flux anomalies (B_{oT}) and to salinity and freshwater flux anomalies (B_{oS}). Dashed blue and red lines represent the cross-term components proportional to temperature and freshwater flux anomalies and to salinity and heat flux anomalies. The black solid line represents the total EPE flux.

are the components correlated to surface buoyancy anomalies. This approximation is useful for scaling the EPE flux mechanism and is explored in the next section.

This analysis suggests the EPE flux in these simulations is well approximated by

$$G_{EPE} \approx \frac{1}{N_r^2}\mathbb{R}\left[\widehat{b_o}^{*}\widehat{B_{oT}}\right]. \tag{16}$$

In the California Current system, the partial T/S compensation means that while the thermal component of the buoyancy flux drives a loss of EPE through the temperature anomalies (b_T), there is also a partially compensating gain of EPE through the correlation of heat flux anomalies and salinity anomalies (b_S). How the EPE flux depends on density compensation more generally is discussed further in section 5 below.

d. Eddy energy reservoirs, conversion rates and fluxes

Changes in the EPE flux have impacts on the EPE reservoir, but also can affect the EKE through the energy conversion terms. The spectra shown in Fig. 4 suggest that, at the surface, the reservoirs of EPE and EKE are both impacted by the response of SST variability in the air-sea energy transfer via EPE flux. Cumulative spectra (or ogives) of the vertically-integrated reservoirs EKE and EPE shown in Fig. 8a,b confirm the same pattern in the mixed-layer integral. The EPE flux drives a sink of EPE to the atmosphere due to SST-induced heat flux anomalies (Fig. 6), which generates a reduction of submesoscale EPE in the mixed-layer of 10 – 25% (Fig. 8a). At the same scales, EKE is also reduced by approximately 10% as seen in Fig. 8b. The EKE reservoir is likely reduced by the smaller rate of eddy energy conversion, namely, vertical buoyancy production ($C_{(EPE,EKE)}$), which decreases significantly (10 – 25%) in the FULL experiment. As mentioned in section 2, $C_{(EPE,EKE)}$ may be attributed to mixed-layer instabilities (and other ageostrophic secondary circulations) where available potential energy stored in thermal-wind balanced fronts is extracted and converted into perturbation flows such as eddies (Capet et al. 2008a; Fox-Kemper et al. 2008) again reflecting the weaker submesoscale in FULL vs SMTH (Fig. 4). This comparative analysis indicates that at the submesoscale, G_{EPE} directly reduces the EPE which induces a lower baroclinic conversion rate ($C_{EKE,EPE}$) and, consequently, a decrease in the EKE reservoir in the mixed layer.

Fig. 8d also depicts the cumulative difference in surface EKE flux (G_{EKE}) between the two models. Loss of EKE is present in both experiments at the submesoscale since the CFB effect is accounted for in the wind stress parameterizations. At the submesoscale, there is a relative decrease in wind work in the FULL experiment of 15-30%, a reduction of the EKE flux driven by SST variability. The ratio between the two wind work spectra shown is approximately one or greater than one in scales smaller than the effective resolution of the simulation and hence not considered in this analysis. Scalings of the CFB mechanism on the wind work indicate a direct

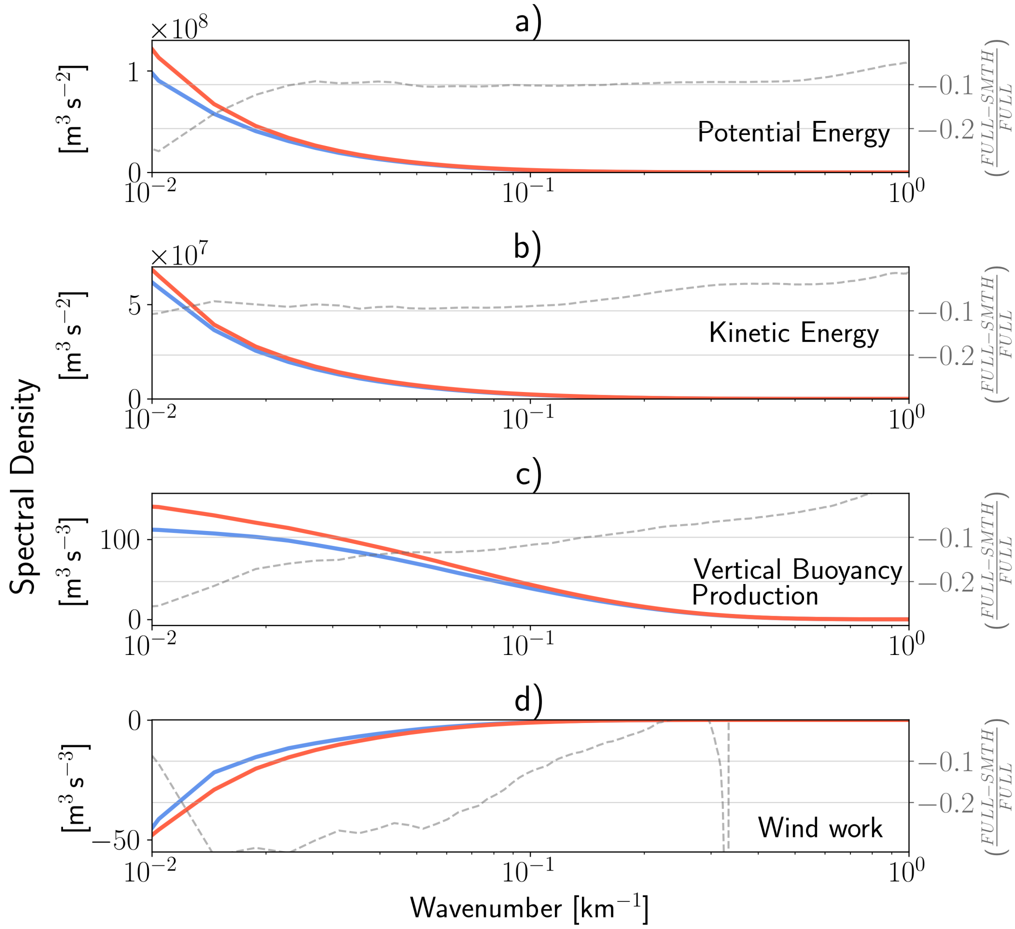

FIG. 8. Cumulative spectra of vertically integrated parameters depict the impact of SST variability in air-sea coupling. Blue (Orange) lines represent the FULL (SMTH) experiment spectra. Ogive graphs are integrated from the larger to smaller horizontal wavenumber. The panels represent (a) Potential Energy, (b) Kinetic Energy, (c) vertical buoyancy production, and (d) wind work. Grey dashed lines indicate the relative difference between the spectra for both experiments. EKE and EPE, and vertical buoyancy production were integrated from 50 m depth to surface, the averaged mixed-layer depth for the region.

relationship between EKE flux and EKE reservoir in the upper ocean (Renault et al. 2017), which is consistent with the decrease of wind work observed in the less energetic FULL experiment (section 5). Concurrently, the TFB mechanism may induce wind anomalies that are partly correlated with surface currents and hence decrease the net loss of EKE by wind work at the submesoscale (Renault et al. 2018; Bai et al. 2023; Conejero et al. 2024). This suggests that the more negative wind work in SMTH experiment is likely due to a combination of the artificial suppression of TFB and the increase of surface EKE due indirectly to the suppressed EPE flux.

A simplified Lorenz diagram summarizing the relative differences in energetics between the two experiments is depicted in Fig. 9. The vertically-integrated energy fluxes, conversion rates, and reservoirs of both experiments indicate that there is a loss of submesoscale eddy energy in the upper ocean due to correlations between surface buoyancy anomalies and buoyancy fluxes (Fig. 5). This reduction of EPE then decreases the EKE indirectly through a reduction in the conversion of EPE to EKE by vertical buoyancy production. Finally, the reduced EKE is associated with a reduction of CFB wind work, which acts at a rate proportional to the EKE (see section 5). While the magnitude of these changes in the experiments utilized here are relatively small, $\mathcal{O}(10\%)$, they are similar to changes in the energetics caused by the CFB mechanism found in prior work in this region (Renault et al. 2018). We discuss the relative importance of these two mechanisms and the role of temperature and salinity variability and compensation in the following section.

5. Discussion

In this work, the EPE flux mechanism is described at the submesoscale where it facilitates the transfer of EPE between the ocean and the atmosphere via correlations between surface buoyancy and buoyancy flux. Such mechanism is previously observed using mesoscale-resolving numerical simulations as described in Ma et al. (2016); Bishop et al. (2017); Guo et al. (2022) and Renault et al. (2023), which affects the energy pathways related to conversion rates and reservoirs of eddy energy. The mechanism described in this work highlights the importance of submesoscale SST variability in driving air-sea fluxes at the same scales and how that may affect the estimation of energy conversion rates, sinks, reservoirs when using numerical simulations. In this section, the limitations of reproducing the EPE flux in numerical models, and the importance of this mechanism relative to other air-sea feedbacks, are discussed.

A hierarchy of coupling parameterizations is used in numerical models in order to reproduce the air-sea fluxes, however some of the strategies may underestimate or even fail to generate surface EPE fluxes. Coupled numerical simulations that use a responsive atmosphere and bulk formulae to reproduce air-sea fluxes that rely on similarity theory (Monin and Obukhov 1954) can reproduce the mechanism studied in this work (e.g., the FULL simulation). Uncoupled models that use a

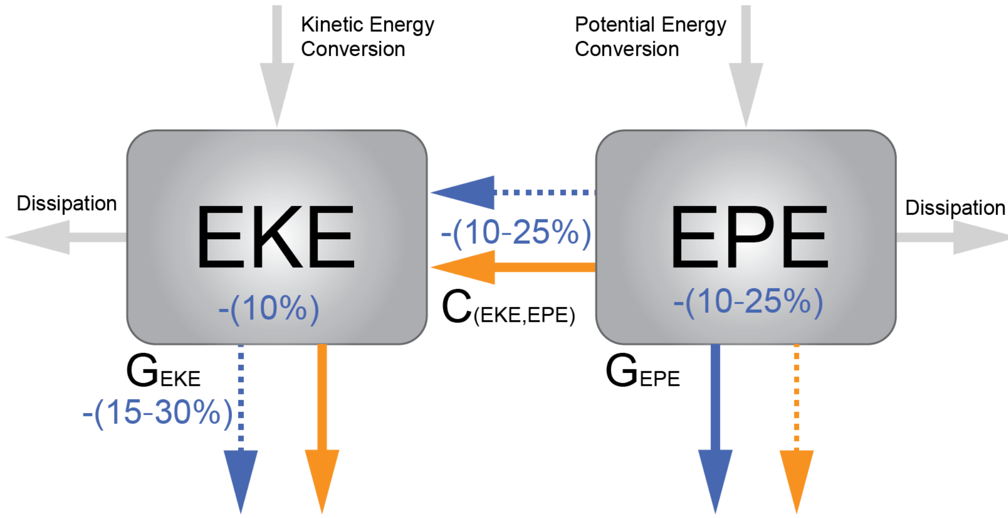

FIG. 9. Sea surface temperature variability at the submesoscale alters the pathways and reservoirs of eddy energy. Simplified Lorenz diagram of the differences in eddy energy reservoirs, fluxes, and conversions. The FULL (SMTH) experiment is illustrated in blue (orange). Differences between the experiments in each component are depicted in terms of the FULL spectra decrease. Fluxes of eddy potential energy (i.e., G_{EPE}) and eddy kinetic energy (i.e., G_{EKE}) are represented by the downward arrows. The reservoirs of eddy potential energy (i.e., EPE) and eddy kinetic energy (i.e., EKE) are represented by the gray boxes. The conversion of EKE to EPE (i.e., $C_{EPE,EKE}$) is represented by the horizontal arrows. Grey arrows represent the cross-scale conversions and dissipation components of energy that are not the focus of this work.

fixed atmosphere, but calculate buoyancy fluxes using parameterizations that depend on SST will likewise generate EPE fluxes, however, it is possible that this flux may not be entirely accurate as the atmosphere cannot evolve in response to these fluxes. However, uncoupled models that use prescribed heat fluxes (a common approach for regional ocean or idealized numerical simulations) fail to generate the mechanism since surface buoyancy fluxes will not respond to surface buoyancy anomalies. In this case, it is anticipated that the modeled submesoscale will be overly energetic (section 4).

One of the approximation strategies for air-sea fluxes used in uncoupled ocean-only models relies on the linearization of parameters, such as heat flux, into climatological (background) and local anomalies (perturbation) components. The climatological components in the heat flux can then be prescribed based on available data or reanalyses, whereas the heat flux anomalies are parameterized as proportional to modeled surface temperature anomalies (Barnier et al. 1995; Ma et al. 2016; Moreton et al. 2021). This linearization is particularly amenable to simple implementation in ocean-only models and may provide a simpler diagnosis of the impact of SST anomalies in the EPE flux. Here, approximations of the heat flux anomaly as a function of SST are obtained in this region at the submesoscale. This linearization of the heat flux anomaly as proportional to the SST anomaly then allows for a further approximation of EPE flux mechanism, described below.

Fig. 10 shows the joint probability distribution for SST and surface heat flux anomalies over the simulation period. For the California Current region, the SST anomalies are mostly correlated to latent and sensible heat flux anomalies at the submesoscale, that is, over 50% of the variance of the portion of the buoyancy flux correlated to buoyancy anomalies is explained by the heat flux components. This allows for the approximation

$$Q'_{net} \approx -\left(Q'_{SH} + Q'_{LH}\right), \tag{17}$$

where Q'_{SH} and Q'_{LH} are the sensible and latent heat flux components, respectively. The spatial anomalies ($'$) obtained in this analysis are computed from the subtraction of a spatial low-pass filter, similar to what is applied in the SST field as described in section 3c, to the variable. The coupling coefficient α_c is computed as the linear regression fit slope from the approximated heat flux (17) and SST spatial anomalies, as shown in Fig. 10. In this work, α_c=31 W m^2 °C^{-1}, which is similar to previous linearizations for the same region at larger scales (Barnier et al. 1995).

As analyzed in section 4b, the correlation between heat flux and surface buoyancy anomalies has the greatest contribution to the submesoscale EPE flux. By invoking the approximation of EPE flux in physical space (Storch et al. 2012) and the linearization of the heat flux obtained in this work (17), an approximate form of the EPE flux is given by

$$G_{EPE} = -\frac{\alpha_\theta \alpha_c g}{N_r^2 \rho_o C_p} b'_o T'_o. \tag{18}$$

This approximation describes EPE flux as the product of surface buoyancy, and can also be further manipulated by approximating buoyancy by the linear equation of state giving

$$G_{EPE} \approx -\frac{1}{N_r^2} \frac{\alpha_C \alpha_\theta^2 g^2}{\rho_o C_p} \left(1 - \frac{1}{R}\right) T_o'^2, \tag{19}$$

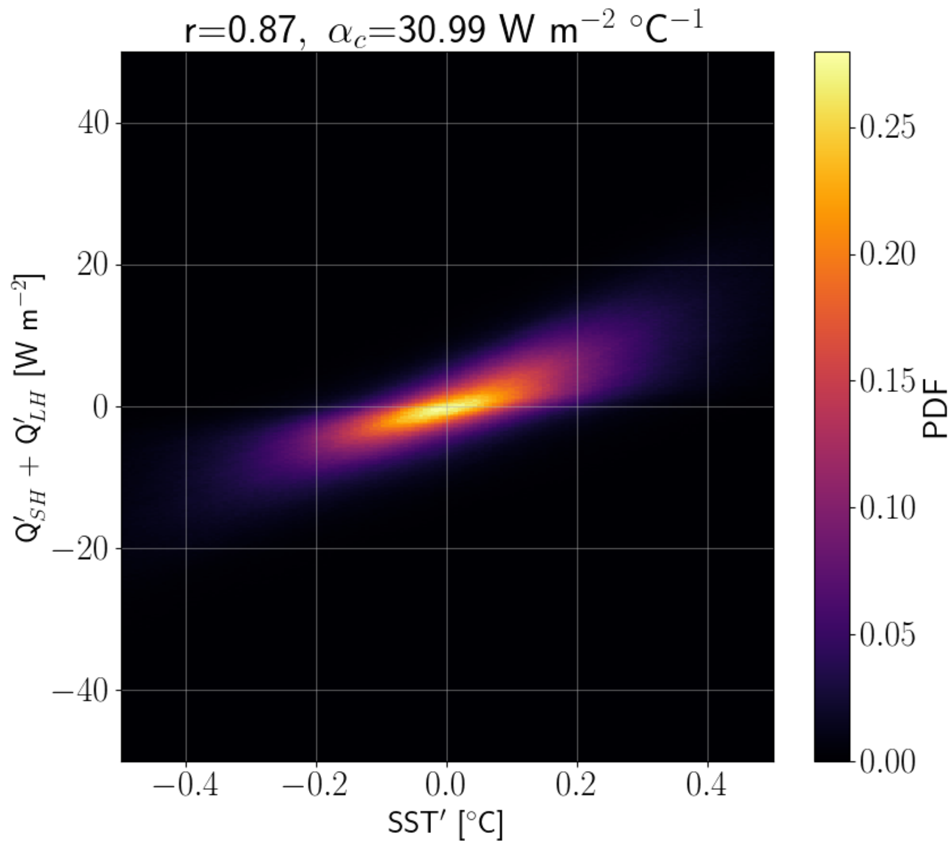

FIG. 10. Two-dimensional histogram of SST and sensible and latent components of the heat flux (Q_{SH+LH}) anomalies in the FULL simulation setup. The impact of SST anomalies in the EPE flux at the submesoscale may be linearized using a coupling coefficient derived from anomalies of SST and non-solar heatflux – proportional to surface buoyancy flux.

where R is the surface density ratio defined as:

$$R = \frac{\alpha_\theta \, T'_o}{\beta_S \, S'_o}. \tag{20}$$

This ratio, R, indicates how temperature and salinity anomalies contribute to the decrease or increase of buoyancy simultaneously. When $R < 0$, the contribution of temperature and salinity anomalies to modulate buoyancy are positively correlated. This scenario favors loss of EPE to the atmosphere as heat flux tends to dissipate buoyancy anomalies (as in Fig. 5), and indeed (21) is strictly negative for $R < 0$. When $R > 0$, the contribution of temperature and salinity anomaly in buoyancy anomalies are negatively correlated, that is, density compensation occurs (Rudnick and Ferrari 1999). Observations suggest some degree of density compensation is ubiquitious in regions with active submesoscales (Rudnick and Martin 2002; Drushka et al. 2019). In compensated fronts, the sign of G_{EPE} is dependent on the relative magnitude of the thermal and salinity components of buoyancy in R. If temperature anomalies determine buoyancy anomalies ($R > 1$) then there is a loss of EPE (as in the simulations here where the median value of the ratio $(1 - R^{-1})^{-1} \approx 0.5$). Conversely, if the salinity component of buoyancy dominates in a compensated front ($0 < R < 1$), such that surface buoyancy fluxes act to increase the density anomalies across the front (ie. the dense side of the front is associated with warm anomalies that are cooled by surface heat fluxes), the EPE will increase due to surface fluxes. This suggests that in some regimes, such as high-latitude β oceans or coastal regions with significant freshwater fluxes, the EPE flux may act as a source of submesoscale energy.

Finally, we note it is also possible to describe G_{EPE} as proportional to the surface EPE reservoir (detailed derivation in Appendix B)

$$G_{EPE} \approx \frac{1}{(1 - \frac{1}{R})} \frac{2 s_b}{\rho_o} EPE_o, \tag{21}$$

where $s_b = -\frac{\alpha_C}{C_p}$ [kg m^{-2} s^{-1}] is the EPE flux coupling coefficient, and and EPE_o is the surface EPE. This form is useful for comparison with the CFB EKE flux, which is proportional to EKE (Renault et al. 2017). The ratio between the two mechanisms can therefore be scaled as

$$\frac{G_{EPE}}{G_{EKE}} \sim \left(\frac{s_b}{s_\tau}\right) \frac{1}{(1 - \frac{1}{R})} \frac{EPE_o}{EKE_o}, \tag{22}$$

where $s_\tau = -3/2 \rho_a C_D |\boldsymbol{U_a}|$ is the wind stress coupling coefficient, C_D is the drag coefficient and $|\boldsymbol{U_a}|$ is the surface wind magnitude. This ratio indicates that the relative impact between the two mechanisms is a function of: (i) the magnitude of both coupling coefficients, (ii) the surface density ratio, and (iii) the ratio of the surface eddy energy reservoirs of the system. The coupling coefficients s_b and s_τ are of similar magnitude considering previous estimates of s_τ using observations (Renault et al. 2017) and of α_c from computations in this work (Fig. 10).

The ratio of EKE_o and EPE_o is scale- and season-dependent due to mesoscale and submesoscale dynamics. For instance, EKE and EPE spectra of Western Boundary Currents such as the Gulf

Stream show that strong baroclinic currents have EKE_o and EPE_o reservoirs of similar magnitude for the winter, whereas in the summer, EKE is larger (Callies et al. 2015). These differences are in part related to mixed-layer instabilities amplified in the wintertime as the mixed-layer depth increases (Fox-Kemper et al. 2008). Observations from the eastern subtropical North Pacific also show EKE and EPE magnitudes to be similar at the mesoscale and submesoscale (Callies and Ferrari 2013). Thus, (22) suggests that the results found here – where the direct EPE flux alters submesoscale energetics in a manner that is quantitatively similar to the surface EKE flux – may be found elsewhere when the EPE_o/EKE_o ratio is large or there is substantial density compensation.

6. Summary and conclusion

In this manuscript, the impact of submesoscale SST variability on the flux of EPE is assessed using two configurations of a fully-coupled model with submesoscale-permitting resolution in the ocean, where one of the numerical experiments (SMTH) suppresses submesoscale SST anomalies in the computation of air-sea fluxes. Comparative analysis between the experiments indicates that modifications to the surface buoyancy flux induced by submesoscale SST variability generate an EPE flux at the air-sea interface which acts as a sink of eddy energy in the upper ocean. In these simulations, this leads to a reduction of the EPE reservoir of 10 – 25% at the submesoscale and the small mesoscale. Associated with this, the rate of conversion to EKE by the vertical buoyancy production ($C_{(EPE,EKE)}$) also decreases by 10 – 25%. This in turn leads to an approximately 10% reduction of submesoscale EKE, and consequently a change in the surface wind work (i.e., CFB; Renault et al. 2018) of 15 – 30%. These changes to submesoscale energy are similar in magnitude to those induced in the same region by the CFB, as well as at larger scales globally (Renault et al. 2018; Bishop et al. 2020).

Linearizations of the turbulent heat flux as a function of SST perturbations at the submesoscale (coupling coefficient α_c) allow for the scaling of the EPE flux at the submesoscale in terms of surface buoyancy and temperature anomalies. The EPE flux may then be described as a function of the surface EPE, analogous to scaling arguments for EKE flux being proportional to EKE reservoir (Renault et al. 2017, 2018), with relative magnitude also dependent on the degree of density compensation (Rudnick and Ferrari 1999). A ratio between the EPE and EKE fluxes results in a term proportional to the ratio between the eddy energy reservoirs, suggesting that the relative importance of the EPE flux and CFB mechanisms in reducing eddy energy will be dependent on the relative sizes of the surface EPE and EKE. In this work considering the California Current region, the EPE flux is a sink of surface EPE at the same magnitude of the CFB mechanism for surface EKE, despite the counteracting effect of the partial salinity compensation found in this region (eg., Fig. 7). In regions where salinity dominates in the density compensation (e.g., $0 < R < 1$ as found at high latitudes or regions with strong freshwater influence), EPE flux may contribute to a gain of EPE hence energizing the submesoscale.

Finally, we note that changes between simulations at scales larger than the SST filter scale were also observed in these experiments, which could indicate a change in the upscale flux of energy from the submesoscale to the mesoscale. However, the limited domain size and integration time period of the numerical model considered here do not allow a robust characterization of changes at larger scales. Looking forward, similar submesoscale-resolving experiments in a larger domain, with varying scales of SST filtering, would provide useful insight into both the direct and cross-scale effects of the EPE flux.

Acknowledgments. This work is a contribution to the S-MODE project (Farrar et al. 2020), an EVS-3 Investigation awarded under NASA Research Announcement NNH17ZDA001N-EVS3 and NASA grants 80NSSC21K0554 and 80NSSC24K0412 awarded under NASA Research Announcement NNH20ZDA001NPO to the University of Maryland, College Park. This work also used the GENCI (project 13051) computing resources and support from I-CASCADE and M-ODYSEA TOSCA-CNES projects.

Data availability statement. No observational data was used in this work. Analysis scripts will be made available via http://github.com upon publication.

APPENDIX A

Eddy Potential Energy Equation in Spectral Space

Consider the buoyancy equation (neglecting horizontal mixing)

$$\frac{\partial b}{\partial t} = -\boldsymbol{u_h}.\nabla_h b - wN^2 + \frac{\partial}{\partial z}\kappa\frac{\partial b}{\partial z}, \tag{A1}$$

where $\boldsymbol{u_h}$=(u,v) is the horizontal velocity vector and ∇_h is the horizontal gradient operator. Decomposing the equation in spectral space in respect to the horizontal wavenumber, (A1) becomes

$$\widehat{\frac{\partial b}{\partial t}} = -\widehat{\boldsymbol{u_h}.\nabla_h b} - \widehat{wN^2} + \frac{\partial}{\partial z}\kappa\widehat{\frac{\partial b}{\partial z}}. \tag{A2}$$

Multiplying (A2) by the complex conjugate of buoyancy, $\widehat{b}^*$, and dividing by a spatially and temporally averaged reference buoyancy frequency, N_r^2, yields

$$\frac{\widehat{b}^*}{N_r^2}\widehat{\frac{\partial b}{\partial t}} = -\frac{\widehat{b}^*}{N_r^2}\widehat{\boldsymbol{u_h}.\nabla_h b} - \widehat{w}\widehat{b}^* + \frac{\widehat{b}^*}{N_r^2}\frac{\partial}{\partial z}\kappa\widehat{\frac{\partial b}{\partial z}}. \tag{A3}$$

where the assumption that horizontal variations of N^2 can be neglected in the calculation of the vertical buoyancy production yielding

$$\frac{\widehat{b}^*}{N_r^2}\widehat{wN^2} \approx \widehat{w}\widehat{b}^*. \tag{A4}$$

This assumption was tested using the numerical simulation and major results were found to be robust to this approximation (Storch et al. 2012). The potential energy equation is then found by taking the real component of (A3) giving

$$\frac{\partial}{\partial t}EPE = \mathbb{R}\Big[-\frac{\widehat{b}^*}{N_r^2}\widehat{\boldsymbol{u_h}.\nabla_h b} - \widehat{w}\widehat{b}^* + \frac{\widehat{b}^*}{N_r^2}\frac{\partial}{\partial z}\kappa\widehat{\frac{\partial b}{\partial z}}\Big]. \tag{A5}$$

For simplicity, two different terms are obtained by further manipulating the last term of the (A5) as follows:

$$\frac{\partial}{\partial t}EPE = \mathbb{R}\Big[-\frac{\widehat{b}^*}{N_r^2}\widehat{\boldsymbol{u_h}.\nabla_h b} - \widehat{w}\widehat{b}^* - \frac{1}{N_r^2}\frac{\partial \widehat{b}^*}{\partial z}\kappa\widehat{\frac{\partial b}{\partial z}} + \frac{\partial}{\partial z}\Big(\frac{\widehat{b}^*}{N_r^2}\kappa\widehat{\frac{\partial b}{\partial z}}\Big)\Big]. \tag{A6}$$

The two last terms in A6 represent the dissipation rate and diffusive vertical transport of EPE, respectively. The mixed-layer balance of potential energy is obtained by integrating (A6) from the surface to the mixed layer depth z_m and using the following surface boundary condition:

$$\widehat{\kappa\frac{\partial b}{\partial z}}\Big|_{z=0} = \widehat{B_o}. \tag{A7}$$

Finally,

$$\begin{aligned}\int_{z_m}^{0} \frac{\partial}{\partial t} EPE\, dz = \mathbb{R}\Bigg\{ \int_{z_m}^{0} \Bigg(-\frac{\widehat{b}^*}{N_r^2}\widehat{\boldsymbol{u_h}.\nabla_h b} - \widehat{w}\widehat{b}^* - \frac{1}{N_r^2}\frac{\partial \widehat{b}^*}{\partial z}\kappa\widehat{\frac{\partial b}{\partial z}} \Bigg)\, dz \\ + \frac{\widehat{b}_o^*\widehat{B}_o}{N_r^2} - \frac{\widehat{b}^*}{N_r^2}\kappa\widehat{\frac{\partial b}{\partial z}}\Bigg|_{z_m} \Bigg\}.\end{aligned} \tag{A8}$$

APPENDIX B

Approximated form of the EPE flux at the submesoscale

The EPE flux is defined as the product of the surface buoyancy and the buoyancy flux anomalies as follows (Bishop et al. 2020; Storch et al. 2012):

$$G_{EPE} = \frac{b'_o\, B'_o}{N_r^2}, \tag{B1}$$

where b'_o and B'_o are defined respectively as:

$$b'_o = \alpha_\theta g T'_o - \beta_s g S'_o, \tag{B2}$$

$$B'_o = \frac{\alpha_\theta g}{\rho_o C_p} Q'_{net} - \beta_s g S'_o [E' - P'], \tag{B3}$$

where the prime symbol ($'$) denotes the anomaly of a given variable. It convenient to describe surface buoyancy perturbations in terms of temperature as follows:

$$b'_o = \alpha_\theta g T'_o (1 - \frac{1}{R}), \tag{B4}$$

where R is the density ratio (defined in (20) and see also Rudnick and Ferrari 1999). Since at the submesoscale the EPE flux from ocean to atmosphere primarily generated by surface heat flux anomalies (Fig. 7), we can combine (B4) and (B3) in (B1) to yield

$$G_{EPE} \approx \frac{1}{N_r^2}\frac{\alpha_\theta^2 g^2}{\rho_o C_p}\Big(1 - \frac{1}{R}\Big)\, T'_o\, Q'_{net}. \tag{B5}$$

As described in section 5, it is further possible to approximate the correlated component of the heat flux anomaly in terms of a coupling coefficient. Q'_{net} may then be described as

$$Q'_{net} \approx -\alpha_C T'_o \tag{B6}$$

Thus G_{EPE} is approximately:

$$G_{EPE} \approx -\frac{1}{N_r^2}\frac{\alpha_C \alpha_\theta^2 g^2}{\rho_o C_p}\left(1-\frac{1}{R}\right) T_o'^2. \tag{B7}$$

Using the definition of eddy potential energy (EPE) in terms of density ratio:

$$EPE_o = \frac{1}{2}\frac{\alpha_\theta^2 g^2}{N_r^2}\left(1-\frac{1}{R}\right)^2 T_o'^2 \tag{B8}$$

and multiplying the term (1-$\frac{1}{R}$) in the numerator and denominator of (B7), the equation can be manipulated further in terms of $b_o'^2$. Thus, (B7) becomes:

$$G_{EPE} \approx \frac{1}{\left(1-\frac{1}{R}\right)}\frac{2s_b}{\rho_o}EPE_o, \tag{B9}$$

where $s_b = -\alpha_C / C_p$ kg m^{-2} s^{-1}.

This takes a form similar to the current feedback effect on the wind work, which can be expressed as (Renault et al. 2017):

$$G_{EKE} \approx \frac{2\,s_\tau}{\rho_o}EKE_o, \tag{B10}$$

where $s_\tau \approx -3/2\rho_a C_D|\boldsymbol{U_a}|$ [kg m^{-2}s^{-1}]. Notably, both G_{EPE} and G_{EKE} can thus be seen to act as linear damping terms in the potential and kinetic energy equations, respectively. The ratio between EPE and EKE flux at the submesoscale is

$$\frac{G_{EPE}}{G_{EKE}} \sim \frac{2\alpha_C}{3\rho_a C_D C_p |\boldsymbol{U_a}|} \frac{1}{\left(1-\frac{1}{R}\right)} \frac{EPE_o}{EKE_o}. \tag{B11}$$

References

Bai, Y., A. F. Thompson, A. B. V. Bôas, P. Klein, H. S. Torres, and D. Menemenlis, 2023: Sub-mesoscale wind-front interactions: The combined impact of thermal and current feedback. *Geophysical Research Letters*, **50**, https://doi.org/10.1029/2023GL104807.

Balwada, D., Q. Xiao, S. Smith, R. Abernathey, and A. R. Gray, 2021: Vertical fluxes conditioned on vorticity and strain reveal submesoscale ventilation. *Journal of Physical Oceanography*, **51 (9)**, 2883–2901.

Barkan, R., M. J. Molemaker, K. Srinivasan, J. C. McWilliams, and E. A. D'Asaro, 2019: The role of horizontal divergence in submesoscale frontogenesis. *Journal of Physical Oceanography*, **49 (6)**, 1593–1618.

Barnier, B., L. Siefridt, and P. Marchesiello, 1995: Thermal forcing for a global ocean circulation model using a three-year climatology of ECMWF analyses. *Journal of Marine Systems*, **6**, 363–380.

Bishop, S. P., R. J. Small, and F. O. Bryan, 2020: The global sink of available potential energy by mesoscale air-sea interaction. *Journal of Advances in Modeling Earth Systems*, **12**, https://doi.org/10.1029/2020MS002118.

Bishop, S. P., R. J. Small, F. O. Bryan, and R. A. Tomas, 2017: Scale dependence of midlatitude air-sea interaction. *Journal of Climate*, **30**, 8207–8221, https://doi.org/10.1175/JCLI-D-17-0159.1.

Callies, J., and R. Ferrari, 2013: Interpreting energy and tracer spectra of upper-ocean turbulence in the submesoscale range (1-200 km). *Journal of Physical Oceanography*, **43**, 2456–2474, https://doi.org/10.1175/JPO-D-13-063.1.

Callies, J., R. Ferrari, J. M. Klymak, and J. Gula, 2015: Seasonality in submesoscale turbulence. *Nature Communications*, **6**, https://doi.org/10.1038/ncomms7862.

Capet, X., J. C. McWilliams, M. J. Molemaker, and A. F. Shchepetkin, 2008a: Mesoscale to submesoscale transition in the California Current system. Part I: Flow structure, eddy flux, and observational tests. *Journal of Physical Oceanography*, **38**, 29–43, https://doi.org/10.1175/2007JPO3671.1.

Capet, X., J. C. McWilliams, M. J. Molemaker, and A. F. Shchepetkin, 2008b: Mesoscale to submesoscale transition in the California Current system. Part II: Frontal processes. *Journal of Physical Oceanography*, **38**, 44–64, https://doi.org/10.1175/2007JPO3672.1.

Chelton, D. B., and S. P. Xie, 2010: Coupled ocean-atmosphere interaction at oceanic mesoscales. *Oceanography*, **23**, 54–69, https://doi.org/10.5670/oceanog.2010.05.

Chereskin, T. K., C. B. Rocha, S. T. Gille, D. Menemenlis, and M. Passaro, 2019: Characterizing the transition from balanced to unbalanced motions in the southern California Current. *Journal of Geophysical Research: Oceans*, **124 (3)**, 2088–2109.

Conejero, C., L. Renault, F. Desbiolles, J. McWilliams, and H. Giordani, 2024: Near-surface atmospheric response to meso-and submesoscale current and thermal feedbacks. *Journal of Physical Oceanography*.

Cronin, M., and J. Sprintall, 2001: Wind and buoyancy-forced upper ocean. *Encyclopedia of Ocean Sciences*, 3219–3226, https://doi.org/10.1006/rwos.2001.0157.

Debreu, L., P. Marchesiello, P. Penven, and G. Cambon, 2012: Two-way nesting in split-explicit ocean models: Algorithms, implementation and validation. *Ocean Modelling*, **49**, 1–21.

Drushka, K., W. E. Asher, J. Sprintall, S. T. Gille, and C. Hoang, 2019: Global patterns of submesoscale surface salinity variability. *Journal of Physical Oceanography*, **49 (7)**, 1669–1685.

Edson, J. B., and Coauthors, 2013: On the exchange of momentum over the open ocean. *Journal of Physical Oceanography*, **43 (8)**, 1589–1610.

Farrar, J. T., and Coauthors, 2020: S-MODE: The Sub-Mesoscale Ocean Dynamics Experiment. *IGARSS 2020-2020 IEEE international geoscience and remote sensing symposium*, IEEE, 3533–3536.

Fox-Kemper, B., R. Ferrari, and R. Hallberg, 2008: Parameterization of mixed layer eddies. Part I: Theory and diagnosis. *Journal of Physical Oceanography*, **38**, 1145–1165, https://doi.org/10.1175/2007JPO3792.1.

Guo, Y., S. Bishop, F. Bryan, and S. Bachman, 2022: A global diagnosis of eddy potential energy budget in an eddy-permitting ocean model. *Journal of Physical Oceanography*, **52 (8)**, 1731–1748.

Iyer, S., K. Drushka, E. J. Thompson, and J. Thomson, 2022: Small-scale spatial variations of air-sea heat, moisture, and buoyancy fluxes in the tropical trade winds. *Journal of Geophysical Research: Oceans*, **127**, https://doi.org/10.1029/2022JC018972.

Johnson, L., C. M. Lee, and E. A. D'Asaro, 2016: Global estimates of lateral springtime restratification. *Journal of Physical Oceanography*, **46**, 1555–1573, https://doi.org/10.1175/JPO-D-15-0163.1.

Large, W. G., J. C. McWilliams, and S. C. Doney, 1994: Oceanic vertical mixing: A review and a model with a nonlocal boundary layer parameterization. *Reviews of geophysics*, **32 (4)**, 363–403.

Ma, X., and Coauthors, 2016: Western boundary currents regulated by interaction between ocean eddies and the atmosphere. *Nature*, **535**, 533–537, https://doi.org/10.1038/nature18640.

Mahadevan, A., E. D. . Asaro, C. Lee, and M. J. Perry, 2012: Eddy-driven stratification initiates North Atlantic spring phytoplankton blooms. *Science*, **337**, 54–58, URL https://www.science.org.

Mauzole, Y., H. Torres, and L.-L. Fu, 2020: Patterns and dynamics of SST fronts in the California Current System. *Journal of Geophysical Research: Oceans*, **125 (2)**, e2019JC015 499.

McWilliams, J. C., 2016: Submesoscale currents in the ocean. *Proceedings of the Royal Society A: Mathematical, Physical and Engineering Sciences*, **472 (2189)**, 20160 117.

Monin, A., and A. Obukhov, 1954: Osnovnye zakonomernosti turbulentnogo peremeshivanija v prizemnom sloe atmosfery (Basic laws of turbulent mixing in the atmosphere near the ground). *Trudy geofiz. inst. AN SSSR*, **24 (151)**, 163–187.

Moreton, S., D. Ferreira, M. Roberts, and H. Hewitt, 2021: Air-sea turbulent heat flux feedback over mesoscale eddies. *Geophysical Research Letters*, **48**, https://doi.org/10.1029/2021GL095407.

Nakanishi, M., and H. Niino, 2006: An improved Mellor–Yamada level-3 model: Its numerical stability and application to a regional prediction of advection fog. *Boundary-Layer Meteorology*, **119**, 397–407.

O'Neill, L. W., D. B. Chelton, and S. K. Esbensen, 2012: Covariability of surface wind and stress responses to sea surface temperature fronts. *Journal of Climate*, **25**, 5916–5942, https://doi.org/10.1175/JCLI-D-11-00230.1.

Renault, L., C. Deutsch, J. C. McWilliams, H. Frenzel, J.-H. Liang, and F. Colas, 2016: Partial decoupling of primary productivity from upwelling in the California Current system. *Nature Geoscience*, **9 (7)**, 505–508.

Renault, L., F. Lemarié, and T. Arsouze, 2019: On the implementation and consequences of the oceanic currents feedback in ocean–atmosphere coupled models. *Ocean Modelling*, **141**, 101 423.

Renault, L., S. Masson, V. Oerder, F. Colas, and J. C. McWilliams, 2023: Modulation of the oceanic mesoscale activity by the mesoscale thermal feedback to the atmosphere. *Journal of Physical Oceanography*, **53**, 1651–1667.

Renault, L., J. C. McWilliams, and J. Gula, 2018: Dampening of submesoscale currents by air-sea stress coupling in the Californian upwelling system. *Scientific Reports*, **8**, https://doi.org/10.1038/s41598-018-31602-3.

Renault, L., J. C. McWilliams, and S. Masson, 2017: Satellite observations of imprint of oceanic current on wind stress by air-sea coupling. *Scientific Reports*, **7**, https://doi.org/10.1038/s41598-017-17939-1.

Rudnick, D. L., and R. Ferrari, 1999: Compensation of horizontal temperature and salinity gradients in the ocean mixed layer. *Science*, **283 (5401)**, 526–529.

Rudnick, D. L., and J. P. Martin, 2002: On the horizontal density ratio in the upper ocean. *Dynamics of atmospheres and oceans*, **36 (1-3)**, 3–21.

Seo, H., A. J. Miller, and J. R. Norris, 2016: Eddy-wind interaction in the California Current System: Dynamics and impacts. *Journal of Physical Oceanography*, **46**, 439–459, https://doi.org/10.1175/JPO-D-15-0086.1.

Seo, H., and Coauthors, 2023: Ocean mesoscale and frontal-scale ocean–atmosphere interactions and influence on large-scale climate: A review. *Journal of Climate*, **36 (7)**, 1981–2013.

Shao, M., and Coauthors, 2019: The variability of winds and fluxes observed near submesoscale fronts. *Journal of Geophysical Research: Oceans*, **124**, 7756–7780, https://doi.org/10.1029/2019JC015236.

Shchepetkin, A. F., 2015: An adaptive, courant-number-dependent implicit scheme for vertical advection in oceanic modeling. *Ocean Modelling*, **91**, 38–69.

Shchepetkin, A. F., and J. C. McWilliams, 2005: The regional oceanic modeling system (ROMS): A split-explicit, free-surface, topography-following-coordinate oceanic model. *Ocean modelling*, **9 (4)**, 347–404.

Skamarock, W. C., and Coauthors, 2019: A description of the advanced research wrf model version 4. *National Center for Atmospheric Research: Boulder, CO, USA*, **145 (145)**, 550.

Skyllingstad, E. D., D. Vickers, L. Mahrt, and R. Samelson, 2007: Effects of mesoscale sea-surface temperature fronts on the marine atmospheric boundary layer. *Boundary-layer meteorology*, **123**, 219–237.

Small, R. J., and Coauthors, 2008: Air-sea interaction over ocean fronts and eddies. *Dynamics of Atmospheres and Oceans*, **45**, 274–319, https://doi.org/10.1016/j.dynatmoce.2008.01.001.

Storch, J. S. V., C. Eden, I. Fast, H. Haak, D. Hernández-Deckers, E. Maier-Reimer, J. Marotzke, and D. Stammer, 2012: An estimate of the Lorenz energy cycle for the World Ocean based on the 1/10° STORM/NCEP simulation. *Journal of Physical Oceanography*, **42**, 2185–2205, https://doi.org/10.1175/JPO-D-12-079.1.

Su, Z., H. Torres, P. Klein, A. F. Thompson, L. Siegelman, J. Wang, D. Menemenlis, and C. Hill, 2020: High-frequency submesoscale motions enhance the upward vertical heat transport in the global ocean. *Journal of Geophysical Research: Oceans*, **125**, https://doi.org/10.1029/2020JC016544.

Su, Z., J. Wang, P. Klein, A. F. Thompson, and D. Menemenlis, 2018: Ocean submesoscales as a key component of the global heat budget. *Nature Communications*, **9**, https://doi.org/10.1038/s41467-018-02983-w.

Sullivan, P. P., J. C. McWilliams, J. C. Weil, E. G. Patton, and H. J. Fernando, 2020: Marine boundary layers above heterogeneous SST: Across-front winds. *Journal of the Atmospheric Sciences*, **77 (12)**, 4251–4275.

Sullivan, P. P., J. C. McWilliams, J. C. Weil, E. G. Patton, and H. J. Fernando, 2021: Marine boundary layers above heterogeneous SST: Alongfront winds. *Journal of the Atmospheric Sciences*, **78 (10)**, 3297–3315.

Valcke, S., 2013: The OASIS3 coupler: A European climate modelling community software. *Geoscientific Model Development*, **6 (2)**, 373–388.

Wenegrat, J. O., 2023: The current feedback on stress modifies the Ekman buoyancy flux at fronts. *Journal of Physical Oceanography*, **53 (12)**, 2737–2749.

Wenegrat, J. O., and R. S. Arthur, 2018: Response of the atmospheric boundary layer to submesoscale sea surface temperature fronts. *Geophysical Research Letters*, **45**, 13,505–13,512, https://doi.org/10.1029/2018GL081034.

Wenegrat, J. O., L. N. Thomas, J. Gula, and J. C. McWilliams, 2018: Effects of the submesoscale on the potential vorticity budget of ocean mode waters. *Journal of Physical Oceanography*, **48 (9)**, 2141–2165.

Yang, H., and Coauthors, 2024: Observations reveal intense air-sea exchanges over submesoscale ocean front. *Geophysical Research Letters*, **51 (2)**, e2023GL106 840.

Zhai, X., and R. J. Greatbatch, 2006: Surface eddy diffusivity for heat in a model of the northwest Atlantic Ocean. *Geophysical research letters*, **33 (24)**.